

# Near-field measurement of infrared coplanar strip transmission line attenuation and propagation constants

Peter M. Krenz<sup>1,\*</sup>, Robert L. Olmon<sup>2,3,5</sup>, Brian A. Lail<sup>4</sup>, Markus B. Raschke<sup>2,5</sup>  
Glenn D. Boreman<sup>1</sup>

<sup>1</sup>College of Optics and Photonics, CREOL, University of Central Florida, Orlando, FL 32816, USA

<sup>2</sup>Department of Chemistry, University of Washington, Seattle, WA 98195, USA

<sup>3</sup>Department of Electrical Engineering, University of Washington, Seattle, WA 98195, USA

<sup>4</sup>Department of Electrical and Computer Engineering, Florida Institute of Technology, Melbourne, FL 32901, USA

<sup>5</sup>Present address: Department of Physics and JILA, University of Colorado, Boulder, CO 80309, USA

\*krenz@knights.ucf.edu

**Abstract:** Impedance matched and low loss transmission lines are essential for optimal energy delivery through an integrated optical or plasmonic nanocircuit. A novel method for the measurement of the attenuation and propagation constants of an antenna-coupled coplanar strip (CPS) transmission line is demonstrated at 28.3 THz using scattering-type scanning near-field optical microscopy. Reflection of the propagating optical wave upon an open-circuit or short-circuit load at the terminal of the CPS provides a standing voltage wave, which is mapped through the associated surface-normal  $E_z$  electric near-field component at the metal-air interface. By fitting the analytical standing wave expression to the near-field data, the transmission line properties are determined. Full-wave models and measured results are presented and are in excellent agreement.

©2010 Optical Society of America

**OCIS codes:** (110.6880) Three-dimensional image acquisition; (180.4243) Near-field microscopy; (260.2110) Electromagnetic optics; (260.3060) Infrared.

---

## References and links

1. A. Alù, and N. Engheta, "Wireless at the nanoscale: optical interconnects using matched nanoantennas," *Phys. Rev. Lett.* **104**(21), 213902 (2010).
2. J.-S. Huang, T. Feichtner, P. Biagioni, and B. Hecht, "Impedance matching and emission properties of nanoantennas in an optical nanocircuit," *Nano Lett.* **9**(5), 1897–1902 (2009).
3. C. T. Middlebrook, P. M. Krenz, B. A. Lail, G. D. Boreman, "Infrared phased-array antenna," *Microw. Opt. Technol. Lett.* **50**(3), 719–723 (2008).
4. J. A. Hutchison, S. P. Centeno, H. Odaka, H. Fukumura, J. Hofkens, and H. Uji-I, "Subdiffraction limited, remote excitation of surface enhanced Raman scattering," *Nano Lett.* **9**(3), 995–1001 (2009).
5. A. V. Akimov, A. Mukherjee, C. L. Yu, D. E. Chang, A. S. Zibrov, P. R. Hemmer, H. Park, and M. D. Lukin, "Generation of single optical plasmons in metallic nanowires coupled to quantum dots," *Nature* **450**(7168), 402–406 (2007).
6. A. Yariv, *Optical Electronics in Modern Communications*, 5th ed. (Oxford University Press, New York, 1997).
7. J. Takahara, S. Yamagishi, H. Taki, A. Morimoto, and T. Kobayashi, "Guiding of a one-dimensional optical beam with nanometer diameter," *Opt. Lett.* **22**(7), 475–477 (1997).
8. A. Alù, and N. Engheta, "Optical nanotransmission lines: synthesis of planar left-handed metamaterials in the infrared and visible regimes," *J. Opt. Soc. Am. B* **23**(3), 571–583 (2006).
9. T. A. Mandviwala, B. A. Lail, and G. D. Boreman, "Characterization of microstrip transmission lines at IR frequencies - Modeling, fabrication and measurements," *Microw. Opt. Technol. Lett.* **50**(5), 1232–1237 (2008).
10. J.-S. Huang, T. Feichtner, P. Biagioni, and B. Hecht, "Impedance matching and emission properties of nanoantennas in an optical nanocircuit," *Nano Lett.* **9**(5), 1897–1902 (2009).
11. T. A. Mandviwala, B. A. Lail, and G. D. Boreman, "Infrared-frequency coplanar striplines: design, fabrication, and measurements," *Microw. Opt. Technol. Lett.* **47**(1), 17–20 (2005).
12. J. Wen, S. Romanov, and U. Peschel, "Excitation of plasmonic gap waveguides by nanoantennas," *Opt. Express* **17**(8), 5925–5932 (2009).
13. A. C. Jones, R. L. Olmon, S. E. Skrabalak, B. J. Wiley, Y. N. N. Xia, and M. B. Raschke, "Mid-IR plasmonics: near-field imaging of coherent plasmon modes of silver nanowires," *Nano Lett.* **9**(7), 2553–2558 (2009).
14. L. Novotny, "Effective wavelength scaling for optical antennas," *Phys. Rev. Lett.* **98**(26), 266802 (2007).

15. R. L. Olmon, P. M. Krenz, A. C. Jones, G. D. Boreman, and M. B. Raschke, "Near-field imaging of optical antenna modes in the mid-infrared," *Opt. Express* **16**(25), 20295–20305 (2008).
16. D. M. Pozar, *Microwave Engineering*, 3rd ed., (J. Wiley, Hoboken, NJ, 2005).
17. M. Rang, A. C. Jones, F. Zhou, Z.-Y. Li, B. J. Wiley, Y. Xia, and M. B. Raschke, "Optical near-field mapping of plasmonic nanoprisms," *Nano Lett.* **8**(10), 3357–3363 (2008).
18. R. Esteban, R. Vogelgesang, J. Dorfmueller, A. Dmitriev, C. Rockstuhl, C. Etrich, and K. Kern, "Direct near-field optical imaging of higher order plasmonic resonances," *Nano Lett.* **8**(10), 3155–3159 (2008).
19. A. Bek, R. Vogelgesang, and K. Kern, "Scanning near-field optical microscope with sub 10-nm resolution," *Rev. Sci. Instrum.* **77**(4), 043703 (2006).
20. F. Keilmann and R. Hillenbrand, "Near-field microscopy by elastic light scattering from a tip," *Philos. Transact. A Math. Phys. Eng. Sci.* **362**(1817), 787–805 (2004).
21. B. C. Wadell, *Transmission Line Design Handbook* (Artech House, Boston, 1991).
22. R. L. Olmon, M. Rang, P. M. Krenz, B. A. Lail, L. V. Saraf, G. D. Boreman, and M. B. Raschke, "Determination of electric field, magnetic field, and electric current distributions of infrared optical antennas: A nano-optical vector network analyzer," *Phys. Rev. Lett.* (to be published).
23. S.-N. Lee, J. I. Lee, W. B. Kim, J. G. Yook, Y.-J. Kim, and S. J. Lee, "Conductor-loss reduction for high-frequency transmission lines based on the magnetorheological-fluid polishing method," *Microw. Opt. Technol. Lett.* **42**(5), 405–407 (2004).
24. J. E. Chan, K. Sivaprasad, and K. A. Chamberlin, "High-frequency modeling of frequency-dependent dielectric and conductor losses in transmission lines," *IEEE Trans. Compon. Packag. Tech.* **30**(1), 86–91 (2007).

## 1. Introduction

An integrated optical or plasmonic nanocircuit consists of three basic components: an optical collector or receiver, a waveguide or transmission line, and a nonlocal nanoscale load in the form of, e.g., a molecule, a plasmonic nanoparticle, a detector, or a re-radiating antenna [1–5]. In particular, the efficient energy transduction through that antenna – transmission-line – load system as provided by an impedance matched and low loss transmission line is essential for optimal delivery of energy to the load. It is furthermore of interest to reduce the size of such a system, therefore prohibiting the use of dielectric waveguides, since their cross-sectional size is limited to a minimum on the order of the guided wavelength [6]. The size of the guiding structure can be reduced by either replacing the dielectric core with a negative index dielectric material to reduce the spatial extent of the guided mode [7], or by replacing the dielectric waveguide by a transmission line. Applying concepts adapted from the radio frequency (RF) regime, the transmission line can be constructed of nanoinductors and nanocapacitors based on metamaterials [8], a metal strip separated from a ground plane by a dielectric standoff layer creating a microstrip [9], or two parallel metal wires forming a coplanar strip (CPS) transmission line. The latter stands out for its structural simplicity and the ease with which it can be integrated with planar antenna designs [10–12].

A lack of detailed understanding of the relationship between geometrical or material parameters, and the corresponding transmission line attenuation and propagation constants has made the practical design of properly matched optical circuits challenging so far. In particular, at optical and infrared (IR) frequencies, transmission lines, typically patterned from thin metal films, are subject to loss resulting from damping associated with a large complex permittivity and surface roughness, and the influence of an inhomogeneous dielectric environment [13,14]. In addition, metals in this frequency range exhibit a high sensitivity to geometrical details, with critical dimensions in the nanometer range, thus on the order of the size of fabrication imperfections. These effects make design of transmission lines in the optical regime using theory alone challenging, and create a need for a systematic experimental approach.

Extending previous efforts based on bolometric measurements [9,11], here we demonstrate the measurement of the attenuation and propagation constants of individual antenna-coupled CPSs at long-wave IR frequencies using scattering-type scanning near-field optical microscopy (*s*-SNOM), which we have previously used to characterize IR dipole antenna modes [13,15]. Reflection of propagating optical excitation upon an open-circuit or short-circuit load at the terminal of the CPS provides a standing wave [16], which is mapped through the phase-sensitive measurement of the associated surface-normal  $E_z$  electric near-field component at the metal-air interface. In addition, with the open and short loads, we provide the first practical steps towards impedance matching in the IR by demonstrating how

the impedance mismatch between the CPS and load is visualized in the resulting standing wave.

## 2. Experiment

CPSs with nominally identical dimensions and therefore nominally identical attenuation and propagation constants are investigated with different antenna and load configurations. A dipole antenna is coupled to the CPS to provide excitation of a propagating mode, which is reflected at either an open-circuit or short-circuit termination to create a standing wave. The different types of terminations do not alter the characteristics of the transmission line, but shift the location of the standing wave maxima and minima.

As control experiments, two devices with identical CPS dimensions and corresponding open-circuit and short-circuit loads, but without dipole antennas, are investigated. The near-field measurements of these devices reveal if the incident radiation couples into the transmission line through pathways other than the antenna.

The CPSs are fabricated on a high resistivity (3 - 6 k $\Omega$ -cm) silicon wafer using standard electron-beam lithography techniques. The four devices are metalized with a 5 nm thick titanium adhesion layer and 105 nm thick layer of electron-beam evaporated gold (atomic force microscope (AFM) topographies of the four fabricated devices are shown in Fig. 3). As shown schematically in Fig. 1, the silicon-air interface defines the  $xy$ -plane and the two parallel conductors of the CPS extend along the  $x$ -axis. The conductors are 5  $\mu\text{m}$  long, 220 nm wide, and are separated by 110 nm. The ends of the conductors are unconnected for the open-circuit termination. The nominally short-circuit load is a 150 nm wide gold strip connecting the ends of the two conductors. The 1.8  $\mu\text{m}$  long and 150 nm wide dipole is parallel to the  $y$ -axis. That antenna length corresponds to a resonant continuous half-wave dipole located at a silicon-air interface [15].

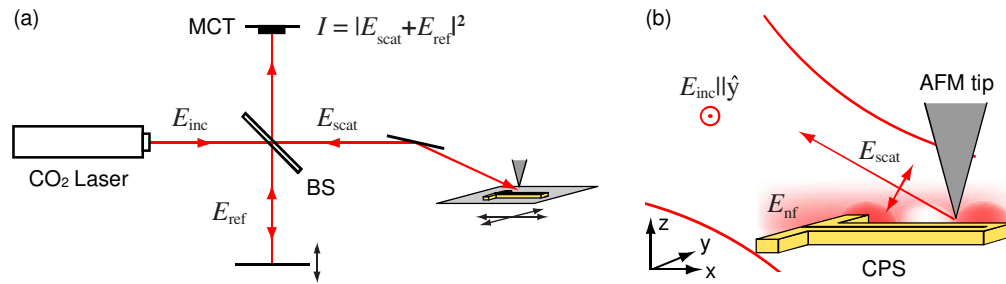


Fig. 1.  $s$ -SNOM measurement setup using interferometric homodyne amplification to determine amplitude and phase of the scattered near-field (a). Magnified view of incident beam illuminating antenna-coupled CPS and AFM tip scattering the near-field distribution (b).

The  $s$ -SNOM measurements are conducted using a modified AFM (CP-Research, Veeco Inc.) operating in dynamic force mode and raster scanning the sample. The CPS devices are illuminated by a CO<sub>2</sub> laser operating at 10.6  $\mu\text{m}$  with polarization in the  $y$ -direction, parallel to the antenna axis. The incident light  $E_{\text{inc}}$  is focused using a Cassegrain objective (NA = 0.5) to a spot size of approximately 30  $\mu\text{m}$  in diameter, propagating in the  $xz$ -plane at a 60° angle with respect to the surface normal. For very large samples, measures must be taken to ensure no phase change occurs at the excitation element. Platinum coated silicon tips (NanoWorld Arrow NCPt) are used to probe the optical near-field  $E_{\text{nf}}$ . Cross-polarized excitation and detection, utilizing the preferential scattering of the tip-parallel  $E_z$  field component, provides minimal tip-sample coupling and thus minimal distortion of the near-field signal [13,17–20]. Polarizing optics are used to control the reference field  $E_{\text{ref}}$  to be polarized parallel to the scattered light  $E_{\text{scat}} \propto E_{z,\text{nf}}$ . The superposition of the back-scattered near-field signal with the

homodyne reference field at the mercury-cadmium-telluride (MCT) photodetector, using a Michelson interferometer, provides phase sensitive imaging [19,20] as shown in Fig. 1(a).

A cross-sectional view of the CPS is shown in Fig. 2 where the simulated electric field is plotted indicating a typical field distribution for our type of transmission line. The  $E_z$  field components on top of the two conductors are equal in magnitude, but  $180^\circ$  out of phase.

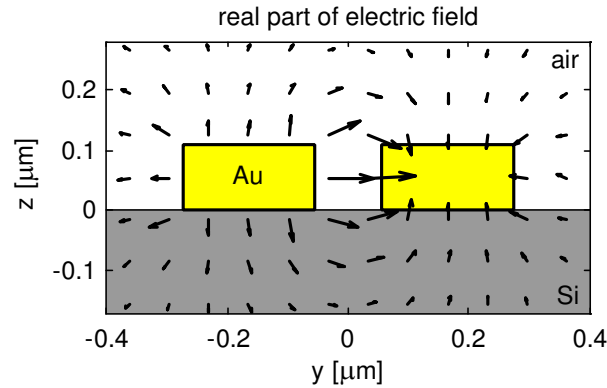


Fig. 2. Cross-section of CPS showing a typical electric field distribution.  $E_z$  components located on top of the conductors are equal in magnitude and  $180^\circ$  out of phase and are measured with *s*-SNOM.

The AFM tip oscillates sinusoidally in the  $z$ -direction and therefore scatters the near-field at different heights. Since the AFM cantilever modulation amplitude is on the length scale of the electric near-field decay length above the sample surface (a few tens of nanometers), which is much less than the wavelength of the incident radiation, lock-in signal demodulation at the cantilever dither frequency or higher harmonics isolates the near-field from the background [13,20]. The background suppression is most efficient the higher the harmonic, but at the cost of a weaker signal. In this experiment, the signal is recorded with a lock-in amplifier that is referenced to the second harmonic of the tip dither frequency.

### 3. Results

The recorded *s*-SNOM images of the four investigated devices are shown in Fig. 3. The CPS with the open-circuit termination but without antenna (a) shows no variation in the measured *s*-SNOM signal, indicating that the incident radiation does not couple into this transmission line configuration. Variations in the measured *s*-SNOM signal of the short-circuit terminated CPS but also without antenna (b) signify that the incident radiation couples into this transmission line configuration, albeit weakly, through the short-circuit load itself, acting as an off-resonant dipole antenna via its elongated gold strip that is parallel to the polarization of the incident radiation.

In contrast, the antenna-coupled CPS sustains strong standing waves of comparable magnitude as shown for both the open-circuit load (c) and the short-circuit load (d). As expected, the standing waves on the adjacent conductors in both cases are out of phase by  $180^\circ$ . The red dashed lines located near  $x = -2 \mu\text{m}$  and  $x = -1 \mu\text{m}$  on the open-circuit and short-circuit loaded CPSs, respectively, indicate an amplitude maximum on one conductor and a minimum on the other conductor.

This phase behavior is further evident from Fig. 4 showing line scans of the measured *s*-SNOM intensity  $I(x)$  (further discussed in section 4 below) of the CPS conductor pairs for the open-circuit (a) and short-circuit (b) loads. In agreement with RF transmission line theory [16], near the load at  $x = 0 \mu\text{m}$  the open-circuit load produces a standing wave amplitude anti-node, while the short-circuit load produces a node, resulting in a  $90^\circ$  phase shift of the voltage standing wave when comparing the two transmission lines.

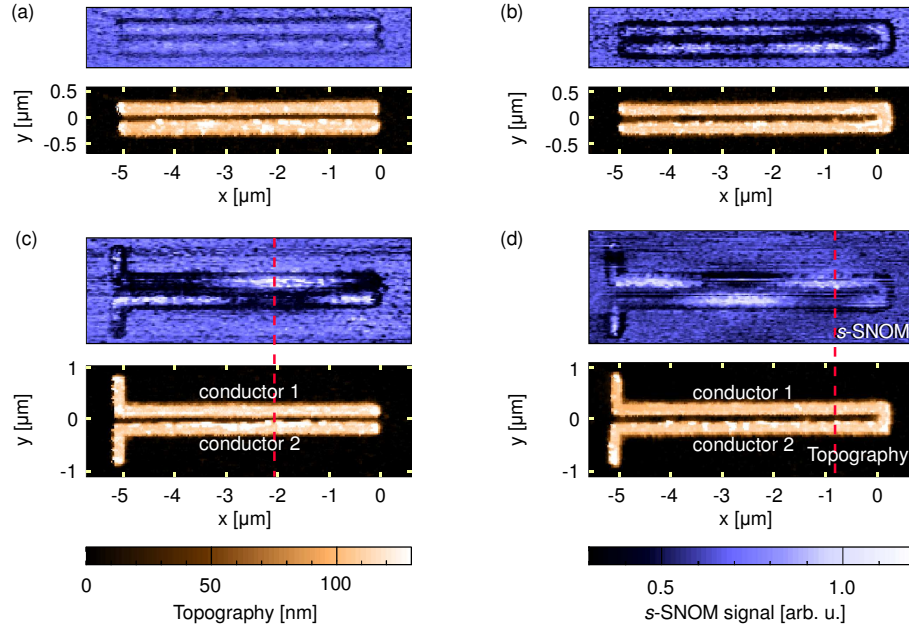


Fig. 3. Measured *s*-SNOM signal (top) and AFM topography (bottom) of fabricated CPSs without antennas, terminated in open-circuit (a) and short-circuit (b) load. Corresponding measurements for antenna-coupled CPSs terminated in open-circuit (c) and short-circuit (d) load. Dashed red lines in (c) and (d) indicate that standing waves on adjacent conductors are 180° out of phase.

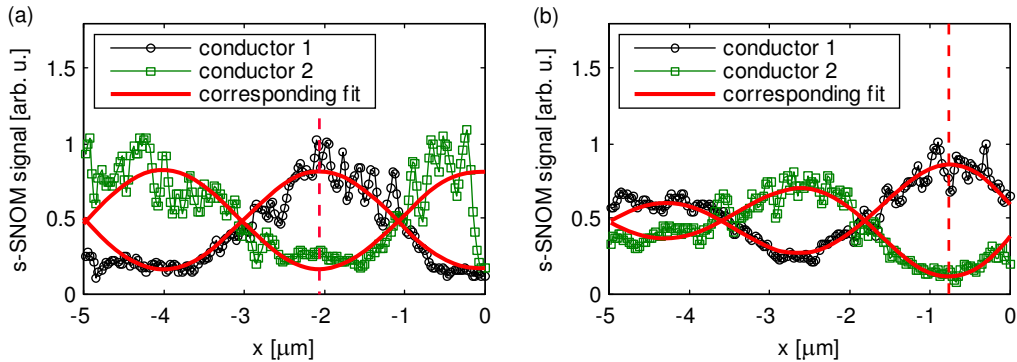


Fig. 4. Measured *s*-SNOM signal along dipole-coupled CPS with open-circuit (a) and short-circuit (b) load. Analytical expression of *s*-SNOM signal is fitted to measurement to determine attenuation and propagation constants of the transmission line. Dashed red lines, corresponding to Figs. 3(c) and 3(d), indicate 180° phase shift between adjacent conductors and 90° phase shift between open-circuit and short-circuit case.

#### 4. Data analysis

The spatial optical near-field variation  $E_{\text{nf}}(x)$  along the transmission line represents a standing wave [16]. It results from the superposition of the forward propagating wave, which emanates from the dipole antenna, and the reflected wave at the impedance mismatched load propagating in opposite direction as described by:

$$E_{\text{nf}}(x) = E_{\text{d}} \left[ e^{-(\alpha + j\beta)x} + \Gamma e^{(\alpha + j\beta)x} \right], \quad (1)$$

where  $E_d$  is the electric field on the transmission line at  $x = 0 \mu\text{m}$ ,  $\alpha$  and  $\beta$  are the attenuation and propagation constants, respectively, and  $\Gamma$  is the reflection coefficient. The propagation constant is related to the wavelength of the guided mode,  $\beta = 2\pi / \lambda_g$ . The guided wavelength is dependent on the structural dimensions of the transmission line and thus may not compare directly with the dipole effective wavelength [14,15,21].

We first analyze the antenna-coupled CPS with the open-circuit termination with  $s$ -SNOM results shown in Fig. 3(c). The recorded  $s$ -SNOM signal  $I(x)$  is related to the standing wave near-field signal  $E_{\text{nf}}(x)$  as described by Eq. (1) for the top and bottom conductors, respectively, as [13, suppl.]:

$$I_{\text{cond.1}}(x) = 2E_{\text{ref}}E_{\text{nf}}(x)A_2 \cos(\Phi_{\text{ref}} - \Phi_{\text{nf}}(x)) + 2E_{\text{nf}}(x)^2 A_0 A_2 + E_{\text{nf}}(x)^2 \frac{A_1^2}{2} + I_{\text{DC}} \quad (2)$$

$$I_{\text{cond.2}}(x) = 2E_{\text{ref}}E_{\text{nf}}(x)A_2 \cos(\Phi_{\text{ref}} - \Phi_{\text{nf}}(x) + \pi) + 2E_{\text{nf}}(x)^2 A_0 A_2 + E_{\text{nf}}(x)^2 \frac{A_1^2}{2} + I_{\text{DC}}. \quad (3)$$

$E_{\text{ref}}$  and  $\Phi_{\text{ref}}$  are the magnitude and phase of the reference beam.  $E_{\text{nf}}$  and  $\Phi_{\text{nf}}$  are the magnitude and phase of the scattered near-field. In accordance with the observation that the scattered  $E_z$  field component on top of the two conductors are equal in magnitude, but  $180^\circ$  out of phase, a  $\pi$  phase shift is added to the scattered near-field of the second conductor. The term  $I_{\text{DC}}$  is added to incorporate a constant offset due to the residual far-field background.  $A_0 - A_2$  are coefficients that depend on the oscillation amplitude of the tip of  $a \approx 20$  nm, the closest distance the tip approaches the sample,  $d \approx 5$  nm, estimated from AFM force-distance measurement, and the approximate exponential decay length of the near-field component of  $d_0 \approx 35$  nm, measured in lift-mode previously [22]. The coefficients  $A_0$ ,  $A_1$ , and  $A_2$  are given by Eqs. (4) – (6) [13, suppl.]

$$A_0 = 1 - \frac{a+d}{d_0} + \frac{2d^2 + 4ad + 3a^2}{4d_0^2}, \quad (4)$$

$$A_1 = -\frac{a}{d_0} + \frac{a(a+d)}{d_0^2}, \quad (5)$$

$$A_2 = \frac{a^2}{4d_0^2}. \quad (6)$$

Equations (2) and (3) are fitted to the measured  $s$ -SNOM signal line traces using a non-linear fitting algorithm that minimizes the sum of squares error, with results shown as a solid line in Fig. 4(a). The attenuation constant, propagation constant, and the reflection coefficient are varied during the fitting procedure and are determined to be  $64.2 \text{ mm}^{-1}$ ,  $1.60 \text{ rad}/\mu\text{m}$ , and  $0.92e^{j0.35}$ , respectively.

For the short-circuit load,  $E_{\text{nf}}(x)$  is the superposition of the wave emanating from the dipole antenna and the weaker wave coupled into the CPS by the short-circuit load given by

$$E_{\text{nf}}(x) = E_d \left[ e^{-(\alpha+j\beta)x} + \Gamma_s e^{(\alpha+j\beta)x} \right] + E_s \left[ e^{-(\alpha+j\beta)(5\mu\text{m}-x)} + \Gamma_d e^{(\alpha+j\beta)(5\mu\text{m}-x)} \right] \quad (7)$$

where  $\Gamma_s$  is the reflection coefficient of the wave reflected by the short-circuit load, and  $\Gamma_d$  is the reflection coefficient of the wave reflected by the dipole. The resulting fit with  $\alpha = 62.4 \text{ mm}^{-1}$ ,  $\beta = 1.53 \text{ rad}/\mu\text{m}$ ,  $\Gamma_s = 0.51e^{j2.62}$ , and  $\Gamma_d = 0.61e^{j4.81}$  is shown in Fig. 4(b).

The standing wave model used for the theoretical fit accurately describes the wave on the transmission lines in general, and thus allows for the determination of the attenuation and propagation constants. However, the model assumes an abrupt termination at each end of the transmission line. With the antenna or load extending the structure of the investigated

transmission lines, the termination is not abrupt, resulting in a deviation between the measurement and model near the terminals [see Figs. 4(a) and 4(b)]. We thus limit the model fit to a truncated section of the transmission line, namely the region from  $-4.5 \mu\text{m}$  to  $-0.5 \mu\text{m}$ , where the model is accurate.

### 5. Simulation of CPS near-field distribution

Ansoft HFSS, which is based on the finite element method, is used to simulate the four CPS configurations investigated as 110 nm thick gold structures located at a silicon-air interface. The relative permittivities used for the simulation at 28.3 THz of gold ( $\epsilon_r' = -4787$  and  $\epsilon_r'' = 1630$ ) and silicon ( $\epsilon_r' = 11.7$  and  $\epsilon_r'' = 1.52 \times 10^{-5}$ ) were measured with a J. A. Woollam IR-VASE ellipsometer. The devices are illuminated by a Gaussian beam with a  $1/e^2$  radius of  $13 \mu\text{m}$  at its focus and an electric-field strength of 1 V/m polarized parallel to the axis of the dipole. The beam is incident onto the device in the  $xz$ -plane, forming a  $60^\circ$  angle with the  $z$ -axis.

The magnitude of the simulated  $E_z$  field 20 nm above one of the conductors of both the antenna-coupled and non-antenna-coupled CPSs terminated in the open-circuit load is plotted in Fig. 5(a). The near-field distribution is only visible on the simulated antenna-coupled CPS as expected and in agreement with the  $s$ -SNOM measurements in Figs. 3(a) and 3(c). The magnitude of Eq. (1), which represents a standing wave that is caused by radiation coupling into the transmission line only through the dipole antenna, is fitted to the magnitude of the simulated  $E_z$  component on the antenna-coupled CPS with the open-circuit termination. The fitted standing wave is also plotted in Fig. 5(a) with the resulting attenuation constant, propagation constant, and reflection coefficient of  $50.7 \text{ mm}^{-1}$ ,  $1.53 \text{ rad}/\mu\text{m}$ , and  $1.00e^{j0.31}$ , respectively.

The magnitude of the simulated  $E_z$  component 20 nm above one of the conductors of the two short-circuit terminated CPSs are shown in Fig. 5(b). In contrast to the open-circuit case, the short-circuit CPS without the antenna possesses a significant field distribution. This is in agreement with the measurements in Fig. 3(b) and the assignment that the load acts like a non-resonant receiving point-dipole antenna. The measured standing wave is not as pronounced as the simulated one, which likely results from the fact that the short-circuit load acts as an off-resonant antenna, and is thus very sensitive to structural imperfections that are not accounted for in the simulations. The near-field distribution above the antenna-coupled CPS is the summation of the standing waves coupling into the transmission line through the dipole antenna and the short-circuit termination as expressed by Eq. (7). The magnitude of Eq. (7) is fitted to the magnitude of the simulated  $E_z$  field component above the antenna-coupled CPS with the short-circuit termination and the resulting fit with  $\alpha = 50.3 \text{ mm}^{-1}$ ,  $\beta = 1.54 \text{ rad}/\mu\text{m}$ ,  $\Gamma_s = 0.94e^{j3.30}$ , and  $\Gamma_d = 0.39e^{j4.29}$  is shown in Fig. 5(b). The median values of the measured attenuation and propagation constants of the nominally identical transmission lines are compared to the corresponding median values of the simulated CPSs in Table 1.

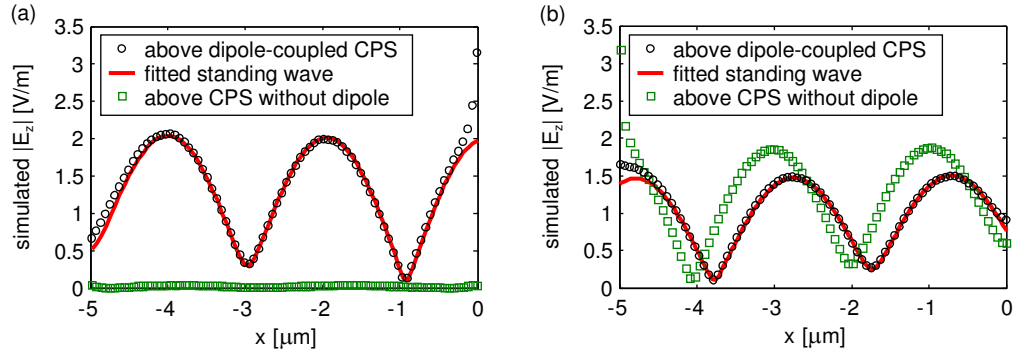


Fig. 5. Simulated magnitude of  $E_z$  on antenna-coupled and non-antenna-coupled CPSs that are terminated in open-circuit (a) and short-circuit (b) loads. Fitted standing wave is also shown. The dipole is located at  $x = -5 \mu\text{m}$  and the load is located at  $x = 0 \mu\text{m}$ .

Figure 5(b) shows that the magnitude of the near-field distribution on the non-antenna-coupled CPS with the short-circuit termination is actually larger than on the antenna-coupled CPS. This is explained by considering that the field distribution on the antenna-coupled transmission line is the summation of the complex fields that form two standing waves, as described by Eq. (7). The complex fields of these standing waves are not in phase and therefore the magnitude of the total field distribution is less than the sum of the magnitude of the individual standing waves.

**Table 1. Median attenuation ( $\alpha$ ) and propagation ( $\beta$ ) constant of measured and simulated antenna-coupled CPSs**

|           | $\alpha$ ( $\text{mm}^{-1}$ ) | $\beta$ ( $\text{rad}/\mu\text{m}$ ) |
|-----------|-------------------------------|--------------------------------------|
| measured  | $63.3 \pm 1.3$                | $1.57 \pm 0.05$                      |
| simulated | $50.5 \pm 0.3$                | $1.54 \pm 0.01$                      |

As seen in Table 1 the simulated and measured propagation constants are in good agreement with each other. The guided wavelengths  $\lambda_g$ , which are calculated from the propagation constants of the measured and simulated CPSs, are  $4.0 \mu\text{m}$  and  $4.1 \mu\text{m}$ , respectively.

The measured attenuation constant is larger than the simulated one. This might be attributable to the approximately  $15 \text{ nm}$  rms surface roughness of the fabricated devices, which is visible in the AFM topographies in Fig. 3, but was not incorporated into the simulations. These surface defects cause localized scattering of the propagating wave leading to a reduction in its magnitude. Experiments in the RF show that transmission lines with surface roughness possess a larger attenuation constant when compared to transmission lines with less or no surface roughness [23,24].

## 6. Conclusion

Infrared radiation was coupled into CPS transmission lines via resonant dipole antennas. Reflection of the optical wave upon an open-circuit or short-circuit load creates a standing wave near-field distribution on the CPS. By imaging the standing wave using  $s$ -SNOM, and fitting the measured data to an analytical expression, we have experimentally determined the attenuation and propagation constants of the CPS.

The measured and simulated propagation constants show good agreement. The measured attenuation constants are slightly larger than the simulated ones, a discrepancy likely attributed to the surface roughness of the fabricated devices. The fabricated CPS can be used for signal transmission with a  $0.55 \text{ dB}$  loss over  $1 \mu\text{m}$  and similar transmission lines have been used as short distance interconnects [3]. These results indicate that near-field measurements using  $s$ -SNOM allows for a quantitative characterization of infrared transmission lines.

The standing wave observed can serve as a measure of the impedance mismatch between the CPS and the load. Reflection of the optical wave upon loads of various impedance would produce correspondingly stronger or weaker standing waves, with those of the open-circuit and short-circuit loads being the most pronounced. The absence of a standing wave would indicate perfect impedance matching between the CPS and the load, and, correspondingly, maximum power transfer. The *s*-SNOM characterization method described here provides a way to determine the relative magnitude of impedance mismatch to practical loads, and thus serves as a design tool enabling integrated infrared antenna systems with high coupling efficiency. The characteristic impedance of the transmission line  $Z_0$  can be determined from the reflection coefficient,  $\Gamma = (Z_L - Z_0)/(Z_L + Z_0)$ , if a load with a known impedance  $Z_L$  is used. If the impedance of the load is unknown, a parametric study of identical CPS with loads of slightly varying geometries can be used to analytically determine the characteristic impedance of the transmission line.